Self-Biased Magnetic Field Sensors Based on Surface Acoustic Waves through Angle-Dependent Magnetoacoustic Coupling

Wenbin Hu [ORCID],[1] Mingxian Huang,[1] Heping Xie,[2] Huaiwu Zhang,[1] and Feiming Bai [ORCID][1,*]

[1] *State Key Laboratory of Electronic Thin Films and Integrated Devices, University of Electronic Science and Technology, Chengdu, 611731, China*

[2] *South-West Institute of Technical Physics, Chengdu, 610054, China*

Surface-acoustic-wave- (SAW) based devices emerge as promising technology in magnetic field sensing by integrating a magnetostrictive layer with the giant $\Delta E/\Delta G$ effect. However, almost all SAW magnetic field sensors require a bias field to obtain high sensitivity. In addition, the true nature of magnetoacoustic coupling still presents a major challenge in understanding and designing this kind of device. Here, a dynamic magnetoelastic model for the $\Delta E/\Delta G$ effect is established in consideration of the important role of the dipole-dipole interaction. The model is also implemented in finite-element-method software to calculate the resonance-frequency responses of multiple fabricated sensors with different ψ angles between the acoustic wave vector and the induced uniaxial magnetic anisotropy. The measured results are in excellent agreement with the simulated ones. A strong resonance-frequency sensitivity (S_{RF}) of 630.4 kHz/Oe is achieved at zero bias field for the device with an optimized ψ angle. Furthermore, the S_{RF} measurements along different directions verify its vector-sensing capability.

I. INTRODUCTION

Magnetic field sensing is critical for many applications, including positioning, navigation, electrical current monitoring, and biomagnetic field detection. Recently, the $\Delta E/\Delta G$ effect was used to detune cantilever [1–3], surface-acoustic-wave (SAW) [4–15], or bulk-acoustic-wave (BAW) [16–19] devices coated with a magnetostrictive film. The ΔE effect is known as the modification of the Young's modulus with respect to a magnetic field. The giant ΔE effect exists in amorphous magnetostrictive materials with high saturation magnetostriction and low anisotropy [20]. Taking SAW devices, for example, the phase velocity of the piezoelectric substrate becomes dispersive upon depositing a magnetic layer onto [4–8] or between [9–13] the interdigital electrodes (IDTs). Similarly, replacing the nonmagnetic IDTs with magnetic ones can also cause a phase velocity or frequency dispersion [14,15]. An ultrahigh dc magnetic field sensitivity of 2.8 Hz/nT and a limit of detection of 800 pT were reported by Li *et al.* using an AlN/Fe-Ga-B resonator [17]. Additionally, a very low magnetic noise level of 100 pT/$\sqrt{\text{Hz}}$ and a bandwidth of 50 kHz were demonstrated by Kittmann *et al.* [11] using a Love-mode delay line. Even higher sensitivity was achieved by Schmalz *et al.* [13] using a Love-mode SAW magnetic field sensor

upon optimizing the pitch width of IDTs. This is because the Love wave, also called a horizontal shear wave, propagates parallel to the magnetic film plane and is thus sensitive to changes of shear modulus (the ΔG effect), which is more pronounced than the ΔE effect under a magnetic field.

However, these attractive sensitivity values are realized by applying certain bias magnetic fields (4 Oe for Fe-Co-Si-B, 12 Oe for Fe-Ga-B, and even 400 Oe for Terfenol-D) [11,17,21]. When used for navigation or biomagnetic applications, a precision range of only a few Gauss or even lower is sufficient. A large bias field inevitably makes a SAW sensor bulky and consumes more power. Although self-biased magnetic sensors were previously reported by Liu *et al.* [5], the nonzero resonance-frequency sensitivity (S_{RF}) was attributed to the relatively high residual magnetic moment and large coercive field, contributing to the nonzero change of the Young's modulus at zero magnetic field. However, a large magnetic hysteresis causes poor sensing linearity. In addition, a true vector sensor is characterized by a highly selective sensitivity to one direction but not to the other vertical directions, which is absent in Ref. [5]. Alternatively, the exchange-bias effect can be employed to design self-biased sensors [3,22]. However, an antiferromagnetic layer can only effectively pin a neighboring ferromagnetic layer below a certain thickness (typically <100 nm), which clearly sets a limit on magnetoacoustic coupling, and thus, the sensitivity of the magnetic field sensors.
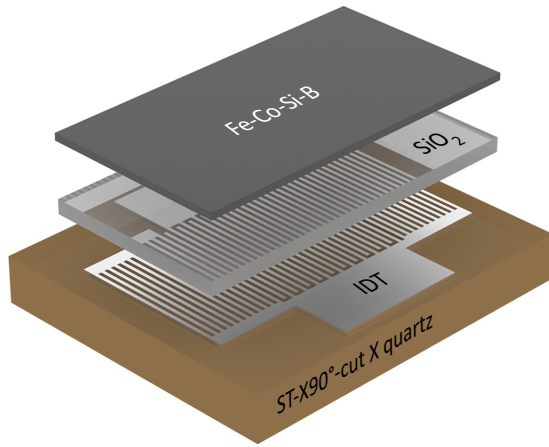
*fmbai@uestc.edu.cn

FIG. 1.   Schematic illustration of multilayered Love-mode SAW resonator.

FIG. 2.   Schematic illustration of the Cartesian coordinates used in the calculation.

Here, we propose a self-biasing approach based on a dynamic magnetoelastic model of the $\Delta E/\Delta G$ effect. Vector SAW magnetic field sensors are designed and fabricated by adjusting the angle between the in-plane-induced uniaxial anisotropy and the SAW propagation direction. A very high S_{RF} of 630.4 kHz/Oe is demonstrated at zero bias field.

This paper is structured as follows. In Sec. II, we provide a dynamic magnetoelastic model for the $\Delta E/\Delta G$ effect (Sec. II A) and a magnetoacoustic finite-element-method (FEM) model of a multilayered SAW structure (Sec. II B) to calculate the resonance-frequency response of SAW magnetic sensors. Then, the methods of device fabrication and measurement are presented in Sec. III. Section IV is devoted to a discussion of the experimental results and the impact of dipole-dipole interactions on the magnetoacoustic coupling (Sec. IV A), which is used to design self-biased vector magnetic field sensors (Sec. IV B).

II. THEORY

Figure 1 shows the configuration of the SAW magnetic field sensor. A ST-X90°-cut quartz is selected as the piezoelectric substrate to generate a Love-mode surface acoustic wave. The acoustic wave is excited by the IDTs deposited on the piezoelectric crystal and resonates from reflections of the short-circuited reflector on both sides. A ferromagnetic Fe-Co-Si-B film is deposited over the entire IDTs and reflector grating, with a SiO$_2$ waveguide layer.

As an important parameter for evaluating device performance, the magnetic field sensitivity of a magnetic SAW resonator can be described as

$$S_{\text{RF}} = \frac{\partial f}{\partial H} = \frac{\partial f}{\partial v}\frac{\partial v}{\partial c}\frac{\partial c}{\partial H}, \tag{1}$$
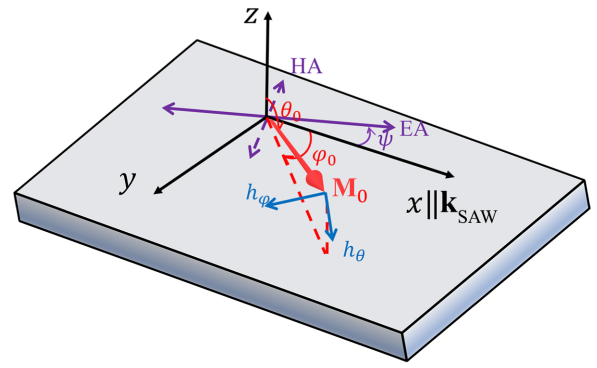
where f, v, and c are the resonance frequency, the phase velocity, and the elastic modulus of the resonator, respectively.

As can be seen, the S_{RF} is determined by three factors. The foremost factor, $\partial c/\partial H$, represents the variation of elastic modulus with an external magnetic field, which is more familiar as the $\Delta E/\Delta G$ effect. $\partial c/\partial H$ arises from magnetostrictive strain, and the static $\Delta E/\Delta G$ effect is modeled in previous works [23–27].

Upon applying an external magnetic field, the phase velocity of the SAW changes due to the variation of the effective elastic modulus of the magnetostrictive-piezoelectric multilayer. The term $\partial v/\partial c$ depends on the ratio between the magnetostrictive-layer thickness and the acoustic wavelength, the acoustic impedance of materials, and the acoustic mode of the structure. In the current multilayered resonator, the Love wave propagates unevenly in each layer, making it difficult to determine $\partial v/\partial c$ by analytical expressions, particularly when coupled with magnetic energy, which increases the complexity of the system. Therefore, a magnetoacoustic coupling model is built in Sec. II B, using the finite-element method.

Finally, the term $\partial f/\partial v$ is determined by the geometric period of the interdigital electrodes. Although magnetostriction also affects the wavelength and causes the resonance-frequency shift, this effect is negligible [28]. So, $\partial f/\partial v$ is equal to $1/\lambda$ in subsequent calculations.

A. Dynamic magnetoelastic model of the ΔG effect

As shown in Fig. 2, a Cartesian coordinate system is built to model the magnetoelastic wave in the ferromagnetic film with the x axis parallel to the acoustic wave vector, $\mathbf{k}_{\text{SAW}}$. Let us consider a spontaneously magnetized ferromagnet,

$$\mathbf{M} = \mathbf{m}M_s, \quad \text{with } |\mathbf{m}| = 1, \tag{2}$$

where M_s is the saturation magnetization and $\mathbf{m}$ is the unit magnetization vector. The internal energy per unit volume

of a magnetic material can be written in the form [29]

$$E_{\text{tot}} = -\mu_0 \mathbf{H} \cdot \mathbf{M} + K(1 - (\mathbf{m} \cdot \mathbf{I})^2) + \frac{1}{2}\mu_0 (\mathbf{N} \cdot \mathbf{M}) \cdot \mathbf{M}$$
$$- \mu_0 \mathbf{h}_{\text{dip}} \cdot \mathbf{M} + E_{\text{ME}} + E_{\text{el}}, \tag{3}$$

where $\mathbf{H}$ is the external magnetic field, K is the first-order uniaxial anisotropy, $\mathbf{I} = (\cos\psi, \sin\psi, 0)$ is the uniaxial anisotropy direction, and $\mathbf{N}$ is a 3×3 demagnetization factor tensor. $\mathbf{h}_{\text{dip}}$ is the dipole-dipole interaction field resulting from the inhomogeneous distribution of magnetic moments in the space. E_{ME} and E_{el} are the magnetoelastic coupling and the elastic energies, respectively, and given by [29]

$$E_{\text{ME}} = B_1(\eta_{11}m_1^2 + \eta_{22}m_2^2 + \eta_{33}m_3^2) + B_2(\eta_{12}m_1 m_2$$
$$+ \eta_{13}m_1 m_3 + \eta_{23}m_2 m_3), \tag{4}$$

$$E_{\text{el}} = \frac{1}{2}c_{ijpq}\eta_{ij}\eta_{pq} \quad i,j,p,q \in \{1,2,3\}. \tag{5}$$

Here, B_1 and B_2 are the magnetoelastic coupling coefficients, and $B_1 = B_2$ for isotropic amorphous films. η_{ij} and η_{pq} are the strain tensors, and c_{ijpq} are the tensors of the elastic constants. In Eq. (5) and below, the repeating indices ($i,\ j,\ p,\ q$) are assumed to be summed.

As we are interested in acoustic wave propagation, we consider only small dynamic perturbations around an equilibrium orientation of magnetic moment:

$$\mathbf{m} = \mathbf{m}_0 + \delta\mathbf{m}, \tag{6}$$

with $\delta\mathbf{m} \ll \mathbf{m}_0$. In spherical coordinates,

$$\mathbf{m}_0 = \begin{pmatrix} \cos\theta_0 \cos\varphi_0 \\ \cos\theta_0 \sin\varphi_0 \\ \sin\theta_0 \end{pmatrix}, \tag{7}$$

$$\delta\mathbf{m} = \begin{pmatrix} \cos\theta_0\cos\varphi_0 & -\sin\theta_0\sin\varphi_0 \\ \cos\theta_0\sin\varphi_0 & \sin\theta_0\cos\varphi_0 \\ -\sin\theta_0 & 0 \end{pmatrix} \begin{pmatrix} \delta\theta \\ \delta\varphi \end{pmatrix}, \tag{8}$$

and the Landau-Lifshitz-Gilbert equation is as follows:

$$\begin{pmatrix} \alpha & -\sin\theta_0 \\ \sin\theta_0 & \alpha\sin^2\theta_0 \end{pmatrix} \begin{pmatrix} \frac{\partial\theta}{\partial t} \\ \frac{\partial\varphi}{\partial t} \end{pmatrix} = -\frac{\gamma}{\mu_0 M_s} \begin{pmatrix} \frac{\partial E_{\text{tot}}}{\partial\theta} \\ \frac{\partial E_{\text{tot}}}{\partial\varphi} \end{pmatrix}, \tag{9}$$

with damping factor α and gyromagnetic ratio γ. $(\theta_0,\ \varphi_0)$ defines the orientation of the magnetic moment in the equilibrium state with minimum local energy. According to the Stoner-Wohlfarth model [30], $(\theta_0,\ \varphi_0)$ can be calculated for any particular $\mathbf{H}$ by finding the zeros of $\partial E_{\text{tot}}/\partial\theta$

(or $\partial E_{\text{tot}}/\partial\varphi$) for $\partial^2 E_{\text{tot}}/\partial\theta^2 > 0$ (or $\partial^2 E_{\text{tot}}/\partial\varphi^2 > 0$). The acoustic perturbation rotates the magnetization to a new θ and φ orientation, where $\theta = \theta_0 + \delta\theta$ and $\varphi = \varphi_0 + \delta\varphi$. $\delta\theta$ and $\delta\varphi$ are the offset angles under the disturbance with $\delta\theta \ll \theta$, $\delta\varphi \ll \varphi$. Consider an infinite magnetic thin film of thickness d with its normal parallel to the z direction (Fig. 2), the dipolar field can be approximated by its average over the film thickness as [31–33]

$$\mathbf{h}_{\text{dip}} = -M_s \left[\left(1 - \frac{1 - e^{-|\mathbf{k}|d}}{|\mathbf{k}|d} \right) \frac{\mathbf{k} \cdot \delta\mathbf{m}}{|\mathbf{k}|^2}\mathbf{k} \right.$$
$$\left. + \frac{1 - e^{-|\mathbf{k}|d}}{|\mathbf{k}|d}(\vec{z} \cdot \delta\mathbf{m})\vec{z} \right], \tag{10}$$

with $\mathbf{k} = \mathbf{k}_{\text{SAW}}$ as the wave vector of the magnetoelastic wave. The spontaneous strains of the ferromagnetic film are considered to be zero because of the constraint of the substrate. Then, E_{tot} can be expanded around the equilibrium position:

$$E_{\text{tot}} = E_0 + \frac{E_{\theta\theta}}{2}\delta\theta^2 + \frac{E_{\varphi\varphi}}{2}\delta\varphi^2 + E_{\theta\varphi}\delta\theta\delta\varphi$$
$$+ E_{\theta\eta_{ij}}\delta\theta\delta\eta_{ij} + E_{\varphi\eta_{ij}}\delta\varphi\delta\eta_{ij}. \tag{11}$$

$E_{\theta\theta}, E_{\varphi\varphi}, E_{\theta\varphi}, E_{\theta\eta_{ij}}$, and $E_{\varphi\eta_{ij}}$ are the second-order derivations of E_{tot} to θ, φ, and η_{ij}, respectively. Making a plane-wave ansatz for offset angles $\delta\theta = \vartheta\exp(i(\mathbf{kr} - \omega t))$ and $\delta\varphi = \Phi\exp(i(\mathbf{kr} - \omega t))$, Eq. (9) can be solved by $\delta\theta$ and $\delta\varphi$ and written as

$$\begin{pmatrix} \delta\theta \\ \delta\varphi \end{pmatrix} = \frac{1}{D} \begin{pmatrix} -\frac{i\omega\alpha}{\gamma}\sin^2\theta_0 - \frac{E_{\varphi\varphi}}{\mu_0 M_s} & -\frac{i\omega}{\gamma}\sin\theta_0 + \frac{E_{\theta\varphi}}{\mu_0 M_s} \\ \frac{i\omega}{\gamma}\sin\theta_0 + \frac{E_{\theta\varphi}}{\mu_0 M_s} & -\frac{i\omega\alpha}{\gamma} - \frac{E_{\theta\theta}}{\mu_0 M_s} \end{pmatrix}$$
$$\times \begin{pmatrix} h_\theta \\ h_\varphi \end{pmatrix}, \tag{12}$$

with

$$D = \left(\frac{i\omega\alpha}{\gamma} + \frac{E_{\theta\theta}}{\mu_0 M_s} \right)\left(\frac{i\omega\alpha}{\gamma}\sin^2\theta_0 + \frac{E_{\varphi\varphi}}{\mu_0 M_s} \right)$$
$$- \left(\frac{\omega}{\gamma}\sin\theta_0 \right)^2 - \frac{E_{\theta\varphi}^2}{(\mu_0 M_s)^2}. \tag{13}$$

As shown in Fig. 2, h_θ and h_φ are the equivalent driving fields of the strain, respectively, along the θ and φ directions:

$$\begin{pmatrix} h_\theta \\ h_\varphi \end{pmatrix} = \frac{1}{\mu_0 M_s} \begin{pmatrix} E_{\theta\eta_{ij}} \\ E_{\varphi\eta_{ij}} \end{pmatrix}\eta_{ij}. \tag{14}$$

Now, we get the offset angles $\delta\theta$ and $\delta\varphi$ caused by an acoustic wave under any initial condition. At this point, a stress-strain constitutive equation of the magnetoelastic

material needs to be found. The Piola-Kirchoff stress tensor can be defined as [34]

$$\sigma_{ij} = \frac{\partial E_{\text{tot}}}{\partial \eta_{ij}} = \frac{\partial E_{\text{el}}}{\partial \eta_{ij}} + \frac{\partial E_{\text{ME}}}{\partial \eta_{ij}} = (c_{ijpq} + \Delta c_{ijpq})\eta_{pq}. \quad (15)$$

As can be seen, the extra magnetoelastic term, E_{ME}, is the source of the ΔG effect, with

$$\Delta c_{ijpq} = \frac{\partial^2 E_{\text{ME}}}{\partial \eta_{ij} \partial \eta_{pq}}. \quad (16)$$

Equation (16) defines the relationship between the elastic tensor and the magnetoelastic energy term. The shear modulus, G, is equivalent to Δc_{1212} (abbreviated as Δc_{66}). If **m** lies within the film plane ($\theta_0 = 90°$), we find the relationship between Δc_{66} of the magnetic film and the local internal energy:

$$\Delta c_{66} = -\frac{B_2^2 \cos^2 2\varphi_0}{\mu_0 M_s D} \left(\frac{i\omega\alpha}{\gamma} + \frac{E_{\theta\theta}}{\mu_0 M_s} \right). \quad (17)$$

In Eq. (17), terms above the quadratic are ignored. Three independent parameters, ω, **H**, and ψ, contribute to the ΔG effect. For frequencies $\omega \ll \omega_s$ (ω_s represents the natural ferromagnetic resonance frequency) and a low α, Eq. (17) can be further reduced to

$$\Delta c_{66}(H, \psi) = -\frac{B_2^2 \cos^2 2\varphi_0}{E_{\varphi\varphi}}, \quad (18)$$

with

$$E_{\varphi\varphi} = \mu_0 \mathbf{H} \cdot \mathbf{M} + 2K \cos 2(\varphi_0 - \psi) + E_{\varphi\varphi}^{\text{ME}}$$
$$+ \mu_0 M_s^2 \left(1 - \frac{1 - e^{-|\mathbf{k}|d}}{|\mathbf{k}|d} \right) \sin^2 \varphi_0. \quad (19)$$

A similar expression to Eq. (19) was reported in Ref. [27], except for the last term, which is critical to the ΔG effect. In Sec. IV, we will discuss the variation trend of Δc_{66} with respect to **H** and ψ in detail.

B. FEM analysis of magnetoacoustic coupling

To illustrate coupling between the elastic wave and the magnetization dynamics in a multilayer structure, a frequency-domain FEM model is built using commercial COMSOL Multiphysics simulation software, which includes the micromagnetics, piezoelectrics, elastic dynamics, and feedback of the magnetostrictive strain from the magnetic system to the elastic system in a fully coupled manner.

ST-X90°-cut quartz is chosen as the piezoelectric substrate with Euler angles (0°, 132.75°, 90°). Aluminum electrodes of 150 nm, a 0.8-μm SiO$_2$ waveguide layer, and a 140-nm-thick Fe-Co-Si-B layer are subsequently

constructed on the ST-X90°-cut quartz. Simulation parameters for the ferromagnetic film come from Ref. [22,35], whereas the rest are available in the COMSOL material library. The length of the piezoelectric substrate is equal to the SAW wavelength, $\lambda = 10$ μm, and its thickness is set as 3λ. A perfectly matched layer and fixed constraints at the bottom prevent interference of body-reflected waves with SAWs. For simplicity, only one acoustic wavelength scale is simulated, and periodic boundary conditions are imposed on both sides of the SAW propagation direction, which corresponds to extending the structure infinitely to both sides.

The elastodynamic process describes the entire system using Newton's equations:

$$-\rho\omega^2 \mathbf{u} = \nabla \cdot \sigma, \quad (20)$$

where ρ and **u** are the material density and the displacement field, respectively. The behavior of ST-X90°-cut quartz follows the linear piezoelectric equation:

$$\sigma = \mathbf{C}^E \eta^{\text{el}} - \mathbf{e}\mathbf{E},$$
$$\mathbf{D} = \mathbf{e}^T \eta^{\text{el}} + \xi \mathbf{E}, \quad (21)$$

where **D** and **E** are the electrical displacement and electric field, respectively. $\mathbf{C}^E$, $\boldsymbol{\xi}$, and **e** are the elastic stiffness, permittivity tensor, and piezoelectric coupling tensor, respectively.

In ferromagnetic films, the damped spin behavior in a magnetic field can be described by micromagnetic Eq. (8). Equations (12) and (14) describe how elastic strain affects the magnetization state, as mentioned in Sec. II A. Furthermore, to determine how magnetization affects the elastic behavior of a ferromagnetic film, Eq. (15) is substituted into Newton Eq. (20) and we obtain

$$-\rho\omega^2 \mathbf{u} = \nabla \cdot \left(\frac{\partial E_{\text{el}}}{\partial \eta} \right) + \nabla \cdot \left(\frac{\partial E_{\text{ME}}}{\partial \eta} \right). \quad (22)$$

Equation (22) contains the contribution of magnetoelastic stress, so the influence of magnetization on the properties of the acoustic waves can be analyzed.

The theoretical formulas above are available in the corresponding solid mechanic and piezoelectric modules, while the micromagnetic equations are developed utilizing weak-form partial differential equation modules, which are coupled to the solid-mechanic modules. This model allows us to analyze magnetoacoustic-electric coupling within the multilayered structure. Additionally, the resonance frequency, deformation, and admittance changes of the structure caused by the magnetic field can be extracted from the eigenfrequency and frequency-domain calculations.
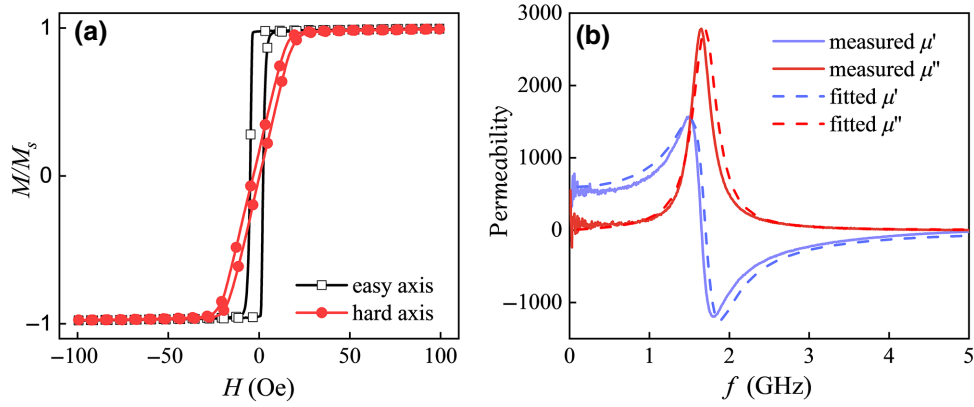
FIG. 3. (a) M-H curves of the Fe-Co-Si-B thin film along the easy axis and hard axis, and (b) measured and fitted permeability spectra from 10 MHz to 5 GHz.

III. METHODS OF DEVICE FABRICATION AND MEASUREMENT

Magnetic SAW resonators are fabricated on ST-X90°-cut quartz substrates. Aluminum IDTs with a thickness of 150 nm are deposited by thermal evaporation and then patterned by a photolithography lift-off process. All resonators consist of 100 pairs of IDTs and two sets of 60-electrode reflectors on each end of the device with a wavelength (λ) of 10 μm and pitch of 200λ. A SiO$_2$ layer is deposited onto IDTs and thinned to a thickness of 800 nm by chemical mechanical polishing. A 140-nm-thick Fe-Co-Si-B film is then deposited on the SiO$_2$ layer by magnetron sputtering using a $(Fe_{90}Co_{10})_{78}Si_{12}B_{10}$ target. An *in situ* magnetic field of about 200 Oe is applied during sputtering to induce in-plane uniaxial anisotropy. Six samples with different angles ($\psi = 0°$, 8°, 22.5°, 45°, 67.5°, and 90°) between the easy axis (EA) and the SAW propagation direction are fabricated, denoted as devices D1–D6.

Figure 3(a) shows the in-plane magnetization versus external magnetic field (M-H) curves for the Fe-Co-Si-B film measured by a vibrating sample magnetometer (BHV-525, Japan). The sample shows a clear EA with an in-plane saturation field, H_k, of about 20 Oe and a low hard-axis (HA) coercive field, H_c, of 1.7 Oe. To obtain the high-frequency properties, we further measure the permeability spectra using a shorted microstrip transmission-line perturbation method [36], as shown in Fig. 3(b). The measured natural ferromagnetic resonance (FMR) frequency is about 1.7 GHz, which is much higher than the operating frequency of SAW resonators. Fitting the imaginary permeability spectrum yields an effective damping factor of $\alpha = 0.009$, which ensures the low FMR loss at the operating frequency.

The frequency response of the SAW resonators upon applying an external magnetic field is measured by tracing the S_{11} scattering parameter using an Agilent network analyzer (N5230A). A rotatable Helmholtz coil driven by a current source (ITECH-6502A) is used to provide a uniform in-plane magnetic field, which is calibrated by a Gauss meter (Lake Shore 425). A continuous magnetic field sweep ranging between +80 and −80 Oe is sufficient to magnetize the Fe-Co-Si-B film to saturation in any measuring direction. All experiments are carried out at room temperature.

IV. RESULTS AND DISCUSSION

A. Field-dependent magnetoacoustic coupling

Figure 4 shows that the S_{11} spectrum of a bare SAW resonator with no magnetic overlayer exhibits a strong
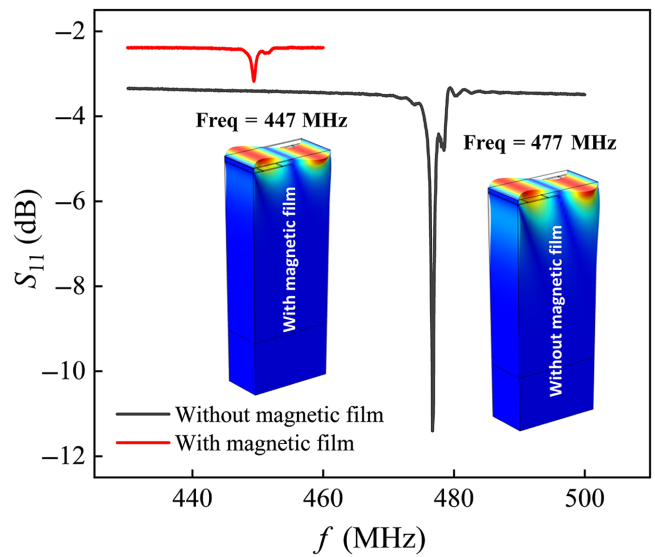

FIG. 4. Measured S_{11} as a function of frequency from SAW resonators with and without Fe-Co-Si-B film. Displacements at resonance frequencies are obtained through COMSOL simulations.

resonance peak at about 477 MHz. The presence of a 140-nm-thick Fe-Co-Si-B layer with $\psi = 0°$ (D1) significantly downshifts the resonance frequency (f_r) to about 447 MHz, due to the lower shear-wave velocity of Fe-Co-Si-B (2821 m/s, calculated by $\sqrt{c_{66}/\rho}$) compared with those of SiO$_2$ and ST-X90°-cut quartz, 3748 and 5047 m/s, respectively. Meanwhile, the amplitude of the resonance peak decays from 8 to 0.9 dB. This can be attributed to the large extra capacitance between the magnetic film and the IDTs, together with the power absorption by the magnetoacoustic coupling [37,38]. FEM simulations show that the displacements of both devices at the resonance frequency can be assigned to the Love-mode resonance.

The magnetoacoustic responses of devices D1 and D6 are then measured upon applying a magnetic field along the HA, as schematically illustrated in the inset of Figs. 5(a) and 5(d). A test cycle consists of three steps: initialization (magnetic field from 0 to 80 Oe), backward sweep (80 to −80 Oe), and forward sweep (−80 to 80 Oe). Despite a small offset caused by hysteresis, the frequency responses of the three sweeps almost overlap, so only the forward sweep is plotted here. Figures 5(a) and 5(d) plot the resonance-frequency shift of devices D1 and D6, respectively, which clearly show the difference between the two devices. A strong ΔG effect is observed for device D1 at low sweeping fields from −15 to +15 Oe, corresponding to a maximum frequency shift (Δf_{max}) of 3.9 MHz. The highest S_{RF} (or df/dH) is about 634 kHz/Oe under an external field of 3.3 Oe. However, the ΔG effect is negligible

for device D6 at low sweeping fields and only becomes much stronger at high fields above ±15 Oe. Δf_{max} is about 6.8 MHz and the highest df/dH reaches 775 kHz/Oe under a field of −16.6 Oe. The frequency response of the former was reported in previous studies [11] and interpreted from a magnetic mean field model, i.e., the angular dispersion of magnetic moments, arising from stray fields, local stresses, or an intrinsic distribution of the easy axis. However, it cannot explain the frequency response or the ΔG effect observed for device D6.

To understand the nature of the resonance-frequency response, FEM simulations are carried out using the magnetoacoustic model in Sec. II. As shown in Figs. 5(b) and 5(e), the displacements and angular distributions of the magnetic moment in the Fe-Co-Si-B film are extracted in the case of $k_{SAW} \parallel M_0$ and $k_{SAW} \perp M_0$. Due to the smaller wavelength of the magnetoelastic wave compared to the film size, magnetic moments are nonuniformly perturbed, leading to a nonzero phase relationship between adjacent magnetic moments. In contrast to Fig. 5(b), a nonzero phase distribution of the magnetic moment perpendicular to k_{SAW} in Fig. 5(e) yields a dipole field, h_{dip}. Using Eqs. (8), (10), and (12), for $\omega \ll \omega_s$, the in-plane component of the dipole field parallel to h_φ can be expressed as

$$h_{\mathrm{dip},\varphi} = -\mu_0 M_s^2 \frac{\sin^2 \varphi_0}{E_{\varphi\varphi}} \left(1 - \frac{1 - e^{-|\mathbf{k}|d}}{|\mathbf{k}|\,d} \right) h_\varphi. \quad (23)$$
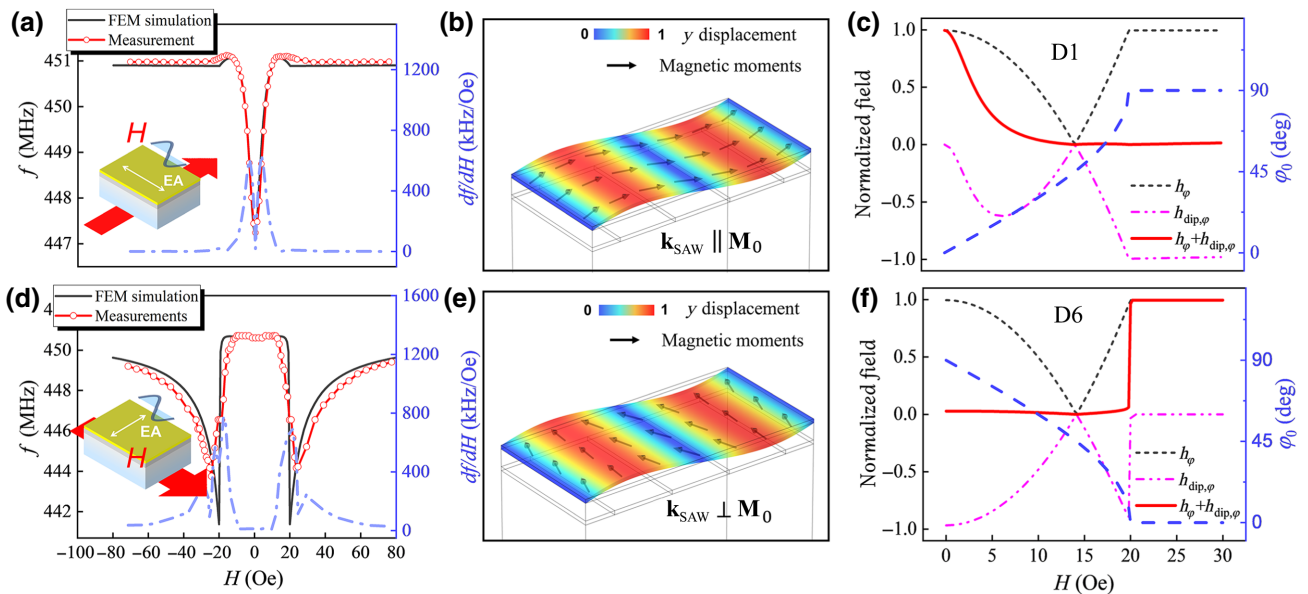

FIG. 5. Results for devices D1 and D6 along HA. (a),(d) Measured and simulated frequency responses as a function of magnetic field. Insets illustrate the measurement setup, where M_0 is parallel to k_{SAW} for D1 but is perpendicular to k_{SAW} for D6, and the sweep field is perpendicular to M_0. (b) Simulated displacements and magnetic moment distributions at resonance frequency. (c),(f) Calculated magnetoelastic driven field h_φ, in-plane dipole field $h_{dip,\varphi}$, and effective perturbation field $h_\varphi + h_{dip,\varphi}$, all of which are normalized. Vertical axis on the right shows the variation of magnetic moment orientation as a function of applied field.
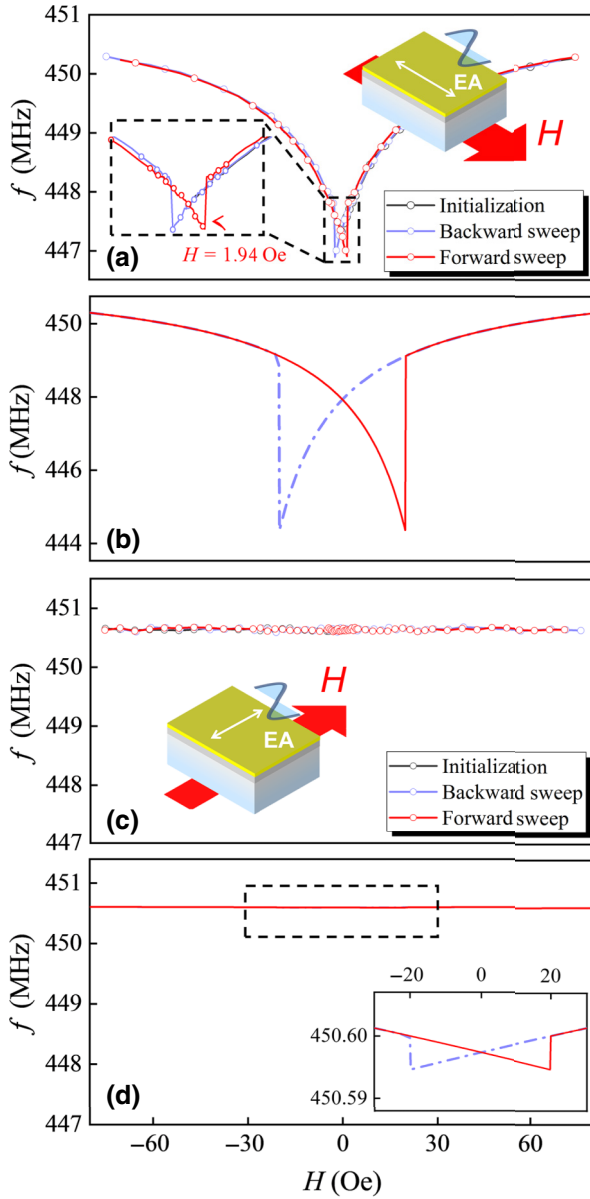
FIG. 6. Measured (a),(c) and simulated (b),(d) frequency responses of devices D1 and D6, respectively, upon applying a field along the EA. Inset shows the amplified frequency response.

Therefore, Eq. (18) can be rewritten as

$$\Delta c_{66} = -\frac{\mu_0 M_s B_2 \cos 2\varphi_0}{\mu_0 \mathbf{H} \cdot \mathbf{M} + 2K \cos 2(\varphi_0 - \psi) + E_{\varphi\varphi}^{ME}}$$

$$\frac{h_\varphi + h_{\mathrm{dip},\varphi}}{\eta_{12}}, \tag{24}$$

where $h_\varphi + h_{\mathrm{dip},\varphi}$ is defined as the effective perturbation field. Normalized h_φ, $h_{\mathrm{dip},\varphi}$, and $h_\varphi + h_{\mathrm{dip},\varphi}$ are calculated as a function of magnetic field $\mathbf{H}$ using Eqs. (14) and (23), and plotted in Figs. 5(c) and 5(f), assuming a constant η_{12}.

As far as **H** is applied along the hard axis, there is a consistent relationship between h_φ and **H** for both devices D1 and D6, but $h_{\mathrm{dip},\varphi}$ heavily depends on the angle (φ_0) between $\mathbf{M}_0$ and $\mathbf{k}_{\mathrm{SAW}}$. When φ_0 is close to 90° [high-field region in Fig. 5(c) and low-field region in Fig. 5(f)], $|h_{\mathrm{dip},\varphi}|$ is significantly enhanced, but when φ_0 is close to 0°, $|h_{\mathrm{dip},\varphi}|$ is reduced to zero. In Fig. 5(f), the sum of h_φ and $h_{\mathrm{dip},\varphi}$ is quite small, in the range of 0 to +20 Oe, leading to a suppressed ΔG effect, according to Eq. (24). As seen in Figs. 5(a) and 5(d), our FEM simulation results (black solid line) are generally in accordance with the experiments.

The measured frequency responses of devices D1 and D6 are also significantly different from each other upon applying a field along the EA. As shown in Fig. 6(a), during both forward and backward sweeps, device D1 exhibits almost a similar magnitude of $\Delta f_{\max}$ to that in Fig. 5(a), and f_r jumps at small magnetic fields (±1.94 Oe). Both of them can be explained by the term $\mu_0 \mathbf{H} \cdot \mathbf{M}$ in Eq. (24), which is enhanced by parallel applied field **H** and reduced by an antiparallel one. Meanwhile, magnetic moments flip 180° upon applying an antiparallel field, causing Δc_{66} to jump near the coercive fields [see Fig. 3(a)]. For device D6 with $\mathbf{k}_{\mathrm{SAW}} \perp \mathbf{M}_0$, the initial magnetic moment orientation, φ_0, is 90° and does not change with the applied field, which corresponds to a large $h_{\mathrm{dip},\varphi}$. This makes the second term $(h_\varphi + h_{\mathrm{dip},\varphi})$ in Eq. (24) very small, and thus, the ΔG effect is attenuated. Figures 6(b) and 6(d) plot the simulated results for devices D1 and D6 upon applying a magnetic field along the EA. According to Fig. 6(d), the amplitude of the frequency response of device D6 is around 2 orders of magnitudes weaker than that of device D1, and thus, is nearly buried by noise. Therefore, almost no frequency response can be observed for device D6 [Fig. 6(c)].

In this section, a dipole field is used to explain the different frequency responses of devices D1 and D6, which are in good agreement with the experimental results. The deviation between the measured and simulated ones, especially between Figs. 6(a) and 6(b), may be attributed to dispersed magnetic moments or magnetic domains, which are not considered in the Stoner-Wohlfarth model. Figures 5(d) and 6(c) demonstrate that device D6 is a true vector magnetic field sensor. However, notice that a bias field of about 16.6 Oe is still required to obtain a high S_{RF}.

B. Angle-dependent magnetoacoustic coupling

We now turn to the resonance-frequency response of devices D2, D3, and D4 ($\psi = 8°$, 22.5°, and 45°, respectively). The measured frequency responses upon applying a magnetic field along the HA are plotted in Figs. 7(a)–7(c). Compared to device D1, devices D2, D3, and D4 show butterflylike frequency-response curves, and the minimum resonance frequency ($f_{\min}$) shifts to the right (left) side during the forward (backward) sweep. A higher
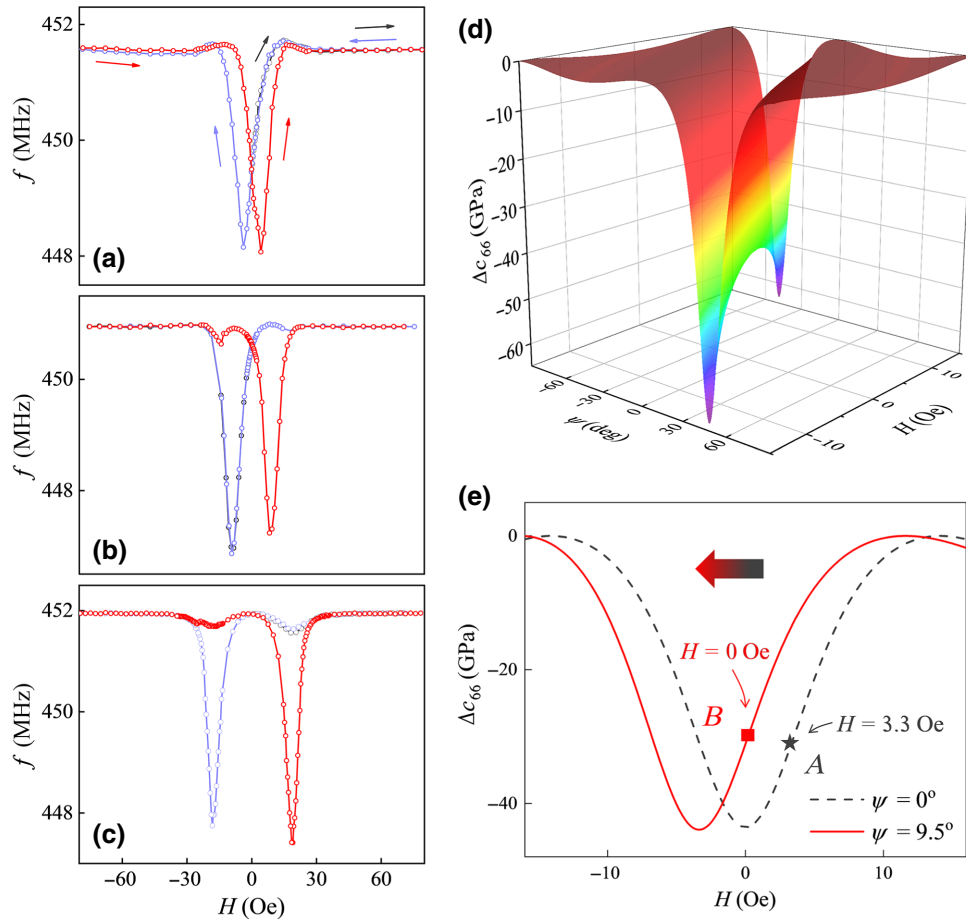
FIG. 7.   Measured frequency responses of devices (a) D2, (b) D3, and (c) D4. (d) Three-dimensional (3D) plot of the calculated dependence of Δc_{66} on ψ and applied field. (e) Calculated variation of Δc_{66} with H when $\psi = 0°$ and $\psi = 9.5°$, respectively. At point A, a magnetic field of 3.3 Oe rotates the magnetic moment orientation, φ_0, from 0° to 9.5°. At point B, magnetic moments are aligned at $\varphi_0 = 9.5°$ under zero bias field by setting $\psi = 9.5°$. All magnetic fields are applied along the HA.

ψ angle leads to a larger $f_{\min}$ offset being seen in Figs. 7(a)–7(c). The steep frequency response at zero field ensures the high sensitivity of these devices, even without a bias field.

In Eq. (24), Δc_{66} exhibits a pronounced φ_0 dependence, which is controlled by both **H** and ψ. In other words, specific magnetization orientation, φ_0, can be referenced to different combinations of (**H**, ψ). Figure 7(d) further plots the 3D dependence of Δc_{66} on the ψ angle and **H** field along the HA. It is clear that, when ψ changes, the minimum point deviates from zero applied field. According to Fig. 5(a), the magnetic moment is rotated to a special φ_0 angle (about 9.5°) by applying a 3.3-Oe magnetic field to maximize df/dH. Likewise, this angle can also be achieved by directly setting $\psi = 9.5°$ during magnetic film deposition. Figure 7(e) plots the calculated Δc_{66} with applied field along the hard axis for $\psi = 0°$ and $\psi = 9.5°$, respectively. The change of ψ from 0° to 9.5° shifts the entire curve from right to left, which is almost equivalent to a bias field of 3.3 Oe, although the magnitude of Δc_{66} is slightly

different. As a result, a nonzero S_{RF} can be obtained at zero bias field.

One obvious strategy to improve the self-biased S_{RF} is to select an appropriate ψ that maximizes $\partial f/\partial H|_{H=0}$. Next, we calculate the relationship between $\partial f/\partial H|_{H=0}$ and ψ in the range of $\psi \in [0°, \ 90°]$. As shown in Fig. 8, self-biased S_{RF} values can be obtained at almost any ψ angles, except 0°, 45°, and 90°, and the highest $\partial f/\partial H|_{H=0}$ appears when $\psi \approx 7°$. As mentioned above, a large $\mathbf{h}_{dip,\varphi}$ suppresses the ΔG effect when ψ ($\psi = \varphi_0$ in this case) is close to 90°. This will deteriorate S_{RF}, thus making it unsuitable to select ψ in the interval [45°, 90°]. We measure the S_{RF} values of devices D1–D6 ($\psi = 0°$, 8°, 22.5°, 45°, 67.5°, and 90°) at zero field, and these are marked in Fig. 8 as well. Again, the measured results are in good agreement with the simulated ones. It should be emphasized that the optimal ψ angle with the maximum self-biased S_{RF} is strongly affected by $\mathbf{h}_{dip}$. For different operating frequencies, magnetostrictive materials, layer thicknesses, or structures of devices, the optimal ψ angle must be recalculated. For
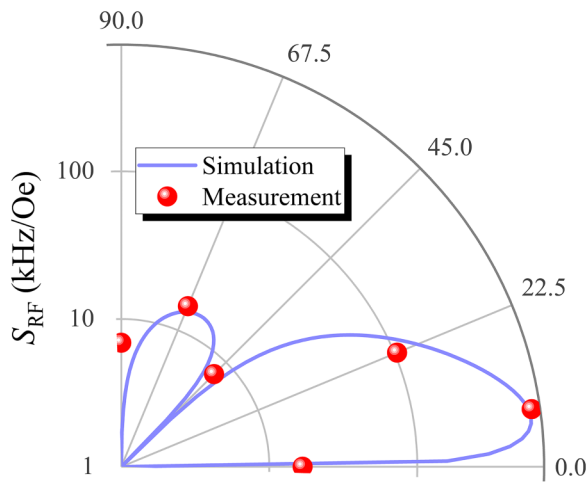
FIG. 8. Simulated and measured ψ angle-dependent S_{RF} at zero bias field. Measurement results are extracted from devices D1–D6, with $\psi = 0°$, 8°, 22.5°, 45°, 67.5°, and 90°, respectively.

example, a 20-nm-thick Fe-Co-Si-B film has an optimal ψ angle of 15° instead of 7°, according to our simulation.

Finally, the magnetic field sensitivity of device D2 is measured along different directions. Figure 9 plots the calculated df/dH and experimental results at zero magnetic field. An "8"-like shape is clearly seen. The angles are referenced to the maximum and minimum S_{RF} located at about 94° and 4°, respectively, slightly off the HA and EA. The measured highest S_{RF} at zero field is about 630.4 kHz/Oe. This demonstrates the ability of our sensor to identify vector magnetic fields. For example, an arbitrary magnetic field direction can be determined by comparing the frequency differences between three vertically
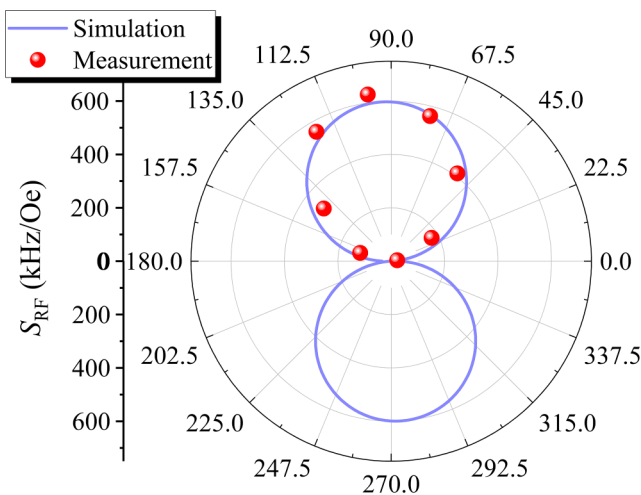

FIG. 9. Simulated and measured S_{RF} results for device D2 at zero magnetic field. Experimental results are obtained by applying an external magnetic field along different directions.

placed sensors, and thus, provides a solid foundation for future array applications of SAW magnetic field sensors.

V. CONCLUSION

A dynamic magnetoelastic model of a thin magnetostrictive film on a piezoelectric substrate is established. The magnetoacoustic coupling is evaluated by measuring the resonance-frequency shift of Love-mode SAW sensors. In comparison with traditional models, our dynamic magnetoelastic model considers the importance of the dipole-dipole interaction and can explain the distinct frequency responses of SAW sensors with different ψ angles between the acoustic wave vector and the in-plane-induced anisotropy. Regulation of the dipole field is achieved by setting an optimized ψ angle during magnetic film deposition, which yields a high S_{RF} of 630.4 kHz/Oe at zero bias field. This approach enables a simple implementation of self-biased SAW magnetic field sensors. Furthermore, the FEM simulation model developed in this work can be used for future investigations of the magnetoacoustic-electric coupling of other types of SAW magnetic field sensors or NEMS magnetoelectric antennas [39].

[1] B. Gojdka, R. Jahns, K. Meurisch, H. Greve, R. Adelung, E. Quandt, R. Knöchel, and F. Faupel, Fully integrable magnetic field sensor based on delta-E effect, Appl. Phys. Lett. **99,** 223502 (2011).

[2] A. V. Turutin, J. V. Vidal, I. V. Kubasov, A. M. Kislyuk, M. D. Malinkovich, Y. N. Parkhomenko, S. P. Kobeleva, O. V. Pakhomov, A. L. Kholkin, and N. A. Sobolev, Magnetoelectric Metglas/bidomain $y + 140°$-cut lithium niobate composite for sensing fT magnetic fields, Appl. Phys. Lett. **112,** 262906 (2018).

[3] B. Spetzler, C. Bald, P. Durdaut, J. Reermann, C. Kirchhof, A. Teplyuk, D. Meyners, E. Quandt, M. Höft, G. Schmidt, and F. Faupel, Exchange biased delta-E effect enables the detection of low frequency pT magnetic fields with simultaneous localization, Sci. Rep. **11,** 5269 (2021).

[4] P. Smole, W. Ruile, C. Korden, A. Ludwig, E. Quandt, S. Krassnitzer, and P. Pongratz, in *Proceedings of the Annual IEEE International Frequency Control Symposium* (2003), pp. 903–906.

[5] X. Liu, B. Tong, J. Ou-Yang, X. Yang, S. Chen, Y. Zhang, and B. Zhu, Self-biased vector magnetic sensor based on a Love-type surface acoustic wave resonator, Appl. Phys. Lett. **113,** 082402 (2018).

[6] X. Liu, J. Ou-Yang, B. Tong, S. Chen, Y. Zhang, B. Zhu, and X. Yang, Influence of the delta-E effect on a surface

acoustic wave resonator, Appl. Phys. Lett. **114,** 062903 (2019).

[7] H. Mishra, J. Streque, M. Hehn, P. Mengue, H. M'Jahed, D. Lacour, K. Dumesnil, S. Petit-Watelot, S. Zhgoon, V. Polewczyk, A. Mazzamurro, A. Talbi, S. Hage-Ali, and O. Elmazria, Temperature compensated magnetic field sensor based on Love waves, Smart Mater. Struct. **29,** 045036 (2020).

[8] H. Mishra, M. Hehn, S. Hage-Ali, S. Petit-Watelot, P. W. Mengue, S. Zghoon, H. M'Jahed, D. Lacour, and O. Elmazria, Microstructured Multilayered Surface-Acoustic-Wave Device for Multifunctional Sensing, Phys. Rev. Appl. **14,** 014053 (2020).

[9] W. Li, P. Dhagat, and A. Jander, Surface acoustic wave magnetic sensor using Galfenol thin film, IEEE Trans. Magn. **48,** 4100 (2012).

[10] H. Zhou, A. Talbi, N. Tiercelin, and O. Bou Matar, Multilayer magnetostrictive structure based surface acoustic wave devices, Appl. Phys. Lett. **104,** 114101 (2014).

[11] A. Kittmann, P. Durdaut, S. Zabel, J. Reermann, J. Schmalz, B. Spetzler, D. Meyners, N. X. Sun, J. McCord, M. Gerken, G. Schmidt, M. Höft, R. Knöchel, F. Faupel, and E. Quandt, Wide band low noise love wave magnetic field sensor system, Sci. Rep. **8,** 278 (2018).

[12] A. Mazzamurro, Y. Dusch, P. Pernod, O. Bou Matar, A. Addad, A. Talbi, and N. Tiercelin, Giant Magnetoelastic Coupling in a Love Acoustic Waveguide Based on TbCo$_2$/FeCo Nanostructured Film on ST-Cut Quartz, Phys. Rev. Appl. **13,** 044001 (2020).

[13] J. Schmalz, A. Kittmann, P. Durdaut, B. Spetzler, F. Faupel, M. Höft, E. Quandt, and M. Gerken, Multi-mode Love-wave SAW magnetic-field sensors, Sensors **20,** 3421 (2020).

[14] M. Elhosnia, O. Elmazriaa, S. Petit-Watelota, L. Bouvota, S. Zhgoonb, A. Talbic, M. Hehna, K. A. Aissaa, S. Hage-Alia, D. Lacoura, F. Sarrya, and O. Boumatar, Magnetic field SAW sensors based on magnetostrictive-piezoelectric layered structures: FEM modeling and experimental validation, Sens. Actuators, A **240,** 41 (2016).

[15] V. PolewczykV, K. Dumesnil, D. Lacour, M. Moutaouekkil, H. Mjahed, N. Tiercelin, S. P. Watelot, H. Mishra, Y. Dusch, S. Hage-Ali, O. Elmazria, F. Montaigne, A. Talbi, O. Bou Matar, and M. Hehn, Unipolar and Bipolar High-Magnetic-Field Sensors Based on Surface Acoustic Wave Resonators, Phys. Rev. Appl. **8,** 024001 (2017).

[16] T. Nan, Y. Hui, M. Rinaldi, and N. X. Sun, Self-biased 215 MHz magnetoelectric NEMS resonator for ultrasensitive dc magnetic field detection, Sci. Rep. **3,** 02115 (2013).

[17] M. Li, A. Matyushov, C. Dong, H. Chen, H. Lin, T. Nan, Z. Qian, M. Rinaldi, Y. Lin, and N. X. Sun, Ultra-sensitive NEMS magnetoelectric sensor for picotesla dc magnetic field detection, Appl. Phys. Lett. **110,** 143510 (2017).

[18] S. Pawar, J. Singh, and D. Kaur, Magnetic field tunable ferromagnetic shape memory alloy-based piezo-resonator, IEEE Electron Device Lett. **41,** 280 (2020).

[19] J. Singh, A. Kumar, and M. Kumar, Highly tunable film bulk acoustic wave resonator based on Pt/ZnO/Fe$_{65}$Co$_{35}$ thin films, IEEE Trans. Ultrason. Ferroelectr. Control **67,** 2130 (2020).

[20] A. Ludwig and E. Quandt, Optimization of the ΔE effect in thin films and multilayers by magnetic field annealing, IEEE Trans. Magn. **38,** 2829 (2001).

[21] A. Piorra, R. Jahns, I. Teliban, J. L. Gugat, M. Gerken, R. Knöchel, and E. Quandt, Magnetoelectric thin film composites with interdigital electrodes, Appl. Phys. Lett. **103,** 032902 (2013).

[22] E. Lage, C. Kirchhof, V. Hrkac, L. Kienle, R. Jahns, R. Knöchel, E. Quandt, and D. Meyners, Exchange biasing of magnetoelectric composites, Nat. Mater. **11,** 523 (2012).

[23] J. D. Livingston, Magnetomechanical properties of amorphous metals, Phys. Status Solidi A **70,** 591 (1982).

[24] P. T. Squire, Phenomenological model for magnetization, magnetostriction and ΔE effect in field-annealed amorphous ribbons, J. Magn. Magn. Mater. **87,** 299 (1990).

[25] P. T. Squire, Domain model for magnetoelastic behaviour of uniaxial ferromagnets, J. Magn. Magn. Mater. **140,** 1829 (1995).

[26] Z. Sárközi, K. Mackay, and J. C. Peuzin, Elastic properties of magnetostrictive thin films using bending and torsion resonances of a bimorph, J. Appl. Phys. **88,** 5827 (2000).

[27] O. Bou Matar, J. F. Robillard, J. O. Vasseur, A. C. Hladky-Hennion, P. A. Deymier, P. Pernod, and V. Preobrazhensky, Band gap tunability of magneto-elastic phononic crystal, J. Appl. Phys. **111,** 054901 (2012).

[28] L. Huang, Q. Lyu, D. Wen, Z. Zhong, H. Zhang, and F. Bai, Theoretical investigation of magnetoelectric surface acoustic wave characteristics of ZnO/Metglas layered composite, AIP Adv. **6,** 015103 (2016).

[29] A. G. Gurevich and G. A. Melkov, *Magnetization Oscillations and Waves* (CRC Press, Boca Raton, Florida, 1996).

[30] C. Tannous and J. Gieraltowski, The Stoner-Wohlfarth model of ferromagnetism, Eur. J. Phys. **29,** 475 (2008).

[31] K. J. Harte, Theory of magnetization ripple in ferromagnetic films, J. Appl. Phys. **39,** 1503 (1968).

[32] B. A. Kalinikos and A. N. Slavin, Theory of dipole-exchange spin wave spectrum for ferromagnetic films with mixed exchange boundary conditions, J. Phys. C: Solid State Phys. **19,** 7013 (1986).

[33] A. Hernández-Mínguez, F. Macià, J. M. Hernàndez, J. Herfort, and P. V. Santos, Large Nonreciprocal Propagation of Surface Acoustic Waves in Epitaxial Ferromagnetic/Semiconductor Hybrid Structures, Phys. Rev. Appl. **13,** 044018 (2020).

[34] H. R. Hamidzadeh, L. Dai, and R. N. Jazar, *Wave Propagation in Solid and Porous Half-Space Media* (Springer, Berlin, 2014), Vol. 9781461492696.

[35] M. Jovičević Klug, L. Thormählen, V. Röbisch, S. D. Toxværd, M. Höft, R. Knöchel, E. Quandt, D. Meyners, and J. McCord, Antiparallel exchange biased multilayers for low magnetic noise magnetic field sensors, Appl. Phys. Lett. **114,** 192410 (2019).

[36] Y. Liu, L. Chen, C. Y. Tan, H. J. Liu, and C. K. Ong, Broadband complex permeability characterization of magnetic thin films using shorted microstrip transmission-Line perturbation, Rev. Sci. Instrum. **76,** 063911 (2005).

[37] L. Dreher, M. Weiler, M. Pernpeintner, H. Huebl, R. Gross, M. S. Brandt, and S. T. B. Goennenwein, Surface acoustic wave driven ferromagnetic resonance in nickel thin films: Theory and experiment, Phys. Rev. B **86,** 134415 (2012).

[38] M. Küß, M. Heigl, L. Flacke, A. Hefele, A. Hörner, M. Weiler, M. Albrecht, and A. Wixforth, Symmetry of the Magnetoelastic Interaction of Rayleigh and Shear Horizontal Magnetoacoustic Waves in Nickel Thin Films on LiTaO$_3$, Phys. Rev. Appl. **15,** 034046 (2021).

[39] T. Nan, *et al.*, Acoustically actuated ultra-compact NEMS magnetoelectric antennas, Nat. Commun. **8,** 296 (2017).